WARWICK
THE UNIVERSITY OF WARWICK

Manuscript version: Author's Accepted Manuscript
The version presented in WRAP is the author's accepted manuscript and may differ from the published version or Version of Record.

Persistent WRAP URL:
http://wrap.warwick.ac.uk/103252

How to cite:
Please refer to published version for the most recent bibliographic citation information. If a published version is known of, the repository item page linked to above, will contain details on accessing it.

Copyright and reuse:
The Warwick Research Archive Portal (WRAP) makes this work by researchers of the University of Warwick available open access under the following conditions.

© 2018 Elsevier. Licensed under the Creative Commons Attribution-NonCommercial-NoDerivatives 4.0 International http://creativecommons.org/licenses/by-nc-nd/4.0/.

Publisher's statement:
Please refer to the repository item page, publisher's statement section, for further information.

For more information, please contact the WRAP Team at: wrap@warwick.ac.uk.

warwick.ac.uk/lib-publications

Role of oxygen in enhanced fatigue cracking in a PM Ni-based superalloy: stress assisted grain boundary oxidation or dynamic embrittlment?

R. Jiang [1, 2*], D. Proprentner [3, 4], M. Callisti [5], B. Shollock [3, 4], X. T. Hu [1], Y. D. Song [1], P. A. S. Reed [2]

[1] College of Energy and Power Engineering, Nanjing University of Aeronautics and Astronautics, Nanjing, 210016, China

[2] Materials Research Group, Department of Mechanical Engineering, University of Southampton, Highfield, Southampton, SO17 1BJ, UK

[3] Advanced Manufacturing and Materials Centre, WMG, University of Warwick, Coventry CV4 7AL, UK

[4] International Digital Laboratory, WMG, University of Warwick, Coventry CV4 7AL, UK

[5] Department of Materials Science and Metallurgy, Cambridge University, 27 Charles Babbage Road, Cambridge, CB3 0FS, United Kingdom

*Corresponding author. Email: rjiang@nuaa.edu.cn

Abstract: The role of oxygen in enhanced fatigue cracking in an advanced Ni-based superalloy for turbine disc application has been evaluated in fatigue crack initiation and propagation stages along with static oxidation tests. It is found that the grain boundary oxide intrusion has a layered structure. The microstructure- and deformation-dependent grain boundary oxidation dominates the fatigue crack initiation and early propagation processes. As the crack propagates, this contribution arising from oxidation damage may gradually be overtaken by dynamic embrittlement processes until the mechanical damage outstrips the oxygen-related damage, resulting in a transition from intergranular to transgranular crack propagation.

Keywords: Ni-based superalloys; fatigue crack initiation; fatigue crack propagation; stress assisted grain boundary oxidation; dynamic embrittlement

1. Introduction

Powder metallurgy (PM) Ni-based superalloys have been widely used for high pressure turbine disc applications in aeroengines due to their excellent mechanical properties and exceptional resistance to environmental damage such as oxidation at elevated temperatures

[1-5]. However, in these more advanced aeroengines, the PM Ni-based superalloys are required to work at higher temperatures to increase turbine inlet temperature for the sake of increasing the thrust-weight ratio and improving the fuel efficiency. This increases the propensity for failure caused by the combined damage processes arising from fatigue-creep-oxidation. Due to the coupled fatigue-creep-oxidation damage, especially under dwell-fatigue conditions, fatigue failure processes are significantly accelerated as indicated by much shorter fatigue lives and/or faster crack propagation rates as reported in the literature [6-17]. Such accelerated fatigue failure processes are usually associated with intergranular fracture resulting from the interaction between grain boundary (GB) oxidation/embrittlement effects and mechanical fatigue processes, and is a function of the microstructures of the investigated disc superalloys and the service conditions [6-9, 15, 16, 18-30]. In the fatigue crack initiation stage, it is believed that oxide cracking can result in crack initiation, which shortens the fatigue life. This is verified in a few studies which show much shorter fatigue life in pre-exposed disc alloys at elevated temperatures than for virgin/unexposed specimens [31-33]. In the crack propagation stage, enhanced intergranular crack propagation in the aggressive environment at elevated temperature is generally ascribed to the mechanism of stress assisted grain boundary oxidation (SAGBO) [6, 7, 16, 20, 25, 34-38] or dynamic embrittlement (DE) [18, 19, 39, 40] at the crack tip. The former is associated with the accelerated formation of oxides along grain boundaries with the assistance of stress at the crack tip. Enhanced intergranular crack propagation is achieved via the grain boundary oxide cracking due to its brittle nature and low fracture toughness. The latter refers to the segregation of oxygen at the nanometre scale at the grain boundary ahead of the crack tip subjected to stress and a corresponding reduction in cohesive strength of the grain boundary, which then in turn accelerates intergranular crack growth.

Extensive studies have been conducted to evaluate the nature of the grain boundary oxides which contribute to this enhanced intergranular fatigue cracking [6, 7, 20, 23, 25, 34, 36-38]. However, many of these studies are limited by problems of preparation of the oxide-containing specimen in the area of interest (i.e. at the crack tip) to allow detailed examination of the oxide nature, as the fatigue cracking itself is a highly localised process. Improvements in characterisation techniques now enable site-specific specimen preparation using focussed ion beam (FIB). Recent studies on the nature of oxides formed under cyclic loads or at sustained loads at the crack tip, using a combination of FIB, energy dispersive X-ray Spectroscopy (EDS) and nano secondary ion mass spectroscopy (SIMS), show the oxides

have layered structures either along the grain boundary or across the grain boundary in disc alloys RR1000 and U720Li [15, 20, 34]. The layered oxides consist of an external Ni/Co oxide layer, an intermediate Cr oxide layer and an inner Al/Ti oxide layer at the oxide/metal interface, and this is given as evidence of SAGBO occurring at the crack tip. However, this is not a universal observation. Viskari and Hörnqvist studied oxidation processes at the crack tip in Inconel 718 using FIB, SIMS and atom probe tomography. No evident oxides formed at the crack tip, indicating that DE was a more likely mechanism responsible for the enhanced intergranular cracking observed [23, 39, 41]. This difference in oxide characterisation results at crack tips in various alloys exhibiting intergranular failure may arise from differences in: (1) composition of disc alloy, (2) crack tip stress/strain state and (3) the crack tip propagation rate. It is expected that higher strain, which is associated with higher defect density [42-44] and a slow crack propagation rate (in terms of *da/dt*), which can provide more oxidation time in a loading cycle, can accumulate more oxidation products at the crack tip [15, 20].

It seems that both SAGBO and DE may occur in the crack tip process zone [15, 18, 20, 41, 45]. At different crack propagation stages, either SAGBO or DE may make the dominant contribution to fatigue crack propagation (FCP), depending on the test temperature, oxygen partial pressure, loading frequency and the crack tip advancement rate (i.e. FCP rate) [7-9, 13, 15, 41, 46]. In addition, it is not unusual to observe a transition from intergranular to transgranular crack propagation in disc alloys as crack length (ΔK) increases, indicating the mechanisms causing crack propagation are FCP rate dependent [8, 9, 15]. In addition, different FCP rates are usually due to different ΔK levels at the crack tips which are also associated with different stress/strain states [16, 24, 47]. It is therefore necessary to link the assessment of the role of oxygen in fatigue cracking to both FCP rate and local stress/strain levels. However, a systematic assessment of the oxides at the crack tip at such different ΔK levels and crack propagation rates is still missing for most superalloys.

In this study, we have extended our previous work [38] on fatigue crack initiation and early crack propagation in one of the latest generation of PM Ni-based superalloys (i.e. Low Solvus, High Refractory (LSHR) alloy [22, 48, 49]), and focused on oxidation processes at the various stages of fatigue cracking and their role in fatigue crack initiation and propagation under dwell-fatigue conditions. In addition, oxidation under sustained load and in a pre-loaded LSHR alloy variant was assessed to evaluate the effect of strain on oxidation

processes. The contribution of SAGBO, DE and mechanical damage to fatigue cracking at different crack propagation stages is discussed.

2. Materials and experimental procedures

2.1 Materials

The composition (in wt.%) of the LSHR alloy studied here is: 20.7 Co, 12.5 Cr, 3.5 Ti, 3.5 Al, 4.3 W, 2.7 Mo, 1.6 Ta, 1.5 Nb, 0.05 Zr, 0.03 C, 0.03 B, bal. Ni. The LSHR alloy was provided by NASA Glenn Research Centre, and was manufactured by standard power metallurgy processing route followed by solution and aging heat treatments. Details of the employed heat treatments can be found in [50]. Three LSHR alloy variants were used in this study, and the statistical data on the sizes of grains, primary γ′ and secondary γ′ in each LSHR alloy variant are shown in Table 1 which have been reported in our previous research [9, 38].

Table 1 Statistical data on sizes of grains, primary γ′ and secondary γ′ in the LSHR variants

Materials ID	Grain size (μm)	Primary γ′ (μm)	Secondary γ′ (nm)	Tests conducted on each LSHR variant
CG LSHR	38.4±18.1	N/A	153± 29	Short fatigue crack test; oxidation in the pre-loaded condition
MG LSHR	19.9±7.8	N/A	221± 28	Long fatigue crack growth test; oxidation under sustained load
FG LSHR	8.1±2.8	1.74±0.48	89± 15	Short fatigue crack test

Note: CG indicates coarse grained, FG indicates fine grained, and MG indicates medium grain size.

2.2 Short fatigue crack test

Interrupted and uninterrupted short fatigue crack bend bar tests were conducted in the CG and FG LSHR alloys at 650 and 725 ^{o}C in air using an Instron 8501 fatigue testing machine. The aim was to investigate fatigue crack initiation and early crack propagation processes particularly assessing the role of oxygen-related damage in both processes. The specimen dimensions can be seen in Fig. 1 (a). The notch has a depth of 1.25 mm with a curvature radius of 2mm. The notch root was ground and then polished down to a 1 μm finish before

being tested. The tests were conducted under three-point bending with a trapezoidal loading waveform of 1-1-1-1 at a load ratio of 0.1. The maximum nominal elastic stress at the notch root was calculated to be 1020 MPa based on simple beam theory for the uncracked ligament. A finite element elastic-plastic simulation shows that this loading condition produces a maximum strain of 0.98% at the notch root. The uninterrupted tests were carried out to establish the overall fatigue life of the LSHR alloy under the investigated conditions, and to determine suitable testing intervals to be used in the interrupted tests. In the interrupted tests, cycling was stopped and a load of 200 N was applied to the specimens throughout the re-heating and cooling processes to hold the specimens in position in the test chamber. Replicas were then made of the notch root at the static mean load used in the fatigue test once the temperature had cooled to 35 - 40 ^{o}C. The interrupted test was stopped when a dominant crack (>1 mm) appeared at the notch root surface. The morphology of the notch root surface was observed by using a field emission gun scanning electron microscopy (FEG-SEM) JEOL JSM 6500F. The morphology of the crack path in the bulk materials was also observed in the SEM after sectioning the specimen from the centre. However, the short crack growth rates were not measured in this study as no valid singular crack growth rate can be obtained due to the substantial amount of grain boundary cracks whose stress fields interact with each other.

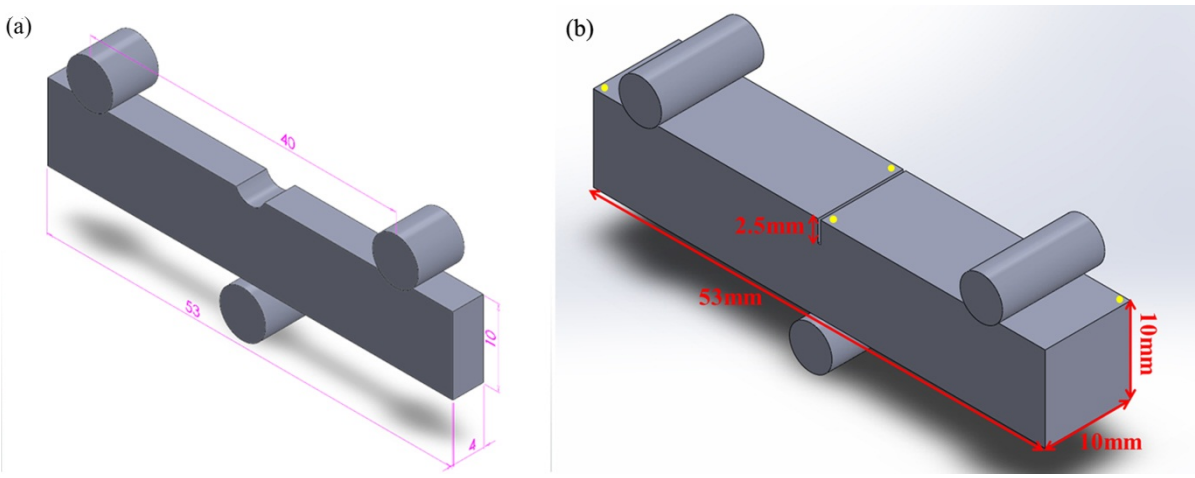

Fig. 1 Specimen dimension and schematic set-up of (a) short fatigue crack test and (b) long fatigue crack growth test. The yellow circular dots in (b) indicate the location of PD wires.

In order to examine oxidation during the crack initiation and propagation stages, transmission electron microscope (TEM) lamellae were extracted (by an in situ lift-out method) from the regions containing the grain boundaries with and without apparent oxides at the notch root surface in the FG LSHR variant test at 725 ^{o}C using a FEI NanoLab Dual

Beam FIB/SEM system. After the lift-out, an in-plane TEM lamella, parallel to the crack propagation direction in the bulk material, was extracted at the crack tip after metallographic sectioning of the specimen. The extracted lamellae were examined in a FEI Tecnai TF20 FEG-TEM with an accelerating voltage of 200 kV. The elemental distribution around the grain boundaries as well as at the interface of the primary γ′/γ matrix was investigated by EDS to reveal the nature of the oxides formed.

2.3 Long fatigue crack growth test

Fatigue crack growth (FCG) tests were conducted followed the guidance of British Standard BS ISO 12108:2002 (i.e. Metallic materials - Fatigue testing - Fatigue crack growth method). The FCG tests were conducted on MG LSHR single edge notched bend (SENB) specimens which have a through thickness notch with a depth of 2.5 mm to evaluate the oxidation at the crack tip at certain ΔK levels. The SENB specimen dimension is shown in Fig. 1 (b). Tests were also conducted under three-point bending using an Instron 8501 fatigue testing machine in air at 725 ^{o}C with a trapezoidal loading waveform of 1-X-1-1 at a load ratio of 0.1 (where X is the hold time at maximum load, X= 90 s and 300 s). The specimen was pre-cracked at room temperature using a load shedding method to a ΔK of ~15 MPa√m. After pre-cracking, the specimen was heated to 725 ^{o}C and then the crack was allowed to propagate under fixed loading amplitude (increasing ΔK levels). Crack length was monitored and recorded by a direct current potential drop (DCPD) method using 4 probe wires. The employed instrument for DCPD measurement is Matelect's DCM-2 model with a pulsed current of 10 A. The current was supplied to the specimen in pulses of constant current and the measurements were taken both during and in between pulse. These were then compared by the unit controller to reduce noise and remove the thermoelectric effects. The FCG rates were derived from the curve of the variation in the electrical potential with time by the secant method.

Oxidation at the propagating crack tip was systematically investigated by using an isotope of oxygen, i.e. $^{18}O_2$. Three scenarios were considered: two evaluated the oxidation processes at a slowly propagating crack tip at 2 different but relatively low ΔK levels of ~16 MPa√m and ~25 MPa√m respectively, with a 300 s dwell at the maximum load. The third scenario evaluated the oxidation at a relatively quickly propagating crack tip (relatively high ΔK level of ~40 MPa√m) with a 90 s dwell at the maximum load. In each case the crack growth was paused at the ΔK levels indicated, and then the pressure of the test chamber was pumped

down to 0.8 bar, followed by refilling with $^{18}O_2$ and N_2 at a ratio of 1:4 up to 1 bar pressure while the specimen was held in the test chamber at the mean testing load. After that, the tests were resumed for a further 5 loading cycles at the same ΔK level of interest in an environment of air + $^{18}O_2$ + N_2 before the tests were stopped. Then the specimens were sectioned through the centre followed by grinding and mechanically polishing, and FEI FIB200-SIMS with a 100 pA Ga+ beam was used to examine the distribution of $^{16}O^-$ and $^{18}O^-$ at the crack tip, to evaluate the levels of oxygen diffusion and the oxidation processes occurring at the crack tip over only a few cycles.

2.4 Sustained load oxidation

Oxidation under sustained load in the MG LSHR alloy variant was conducted on plain bend bar specimens tested at 725 ^{o}C under three point bending. The specimen dimensions are 53 mm × 4 mm × 4 mm. The applied load was used to achieve a maximum strain of ~0.9% on the top central surface in the specimen based on a FE elastic-plastic simulation. The specimen top surface was polished before oxidation to better observe the oxidation products. The specimens were taken out at intervals during the test to observe the successive grain boundary oxidation processes in SEM, and the evolution of grain boundary oxides was recorded. To allow a better understanding of the role of grain boundary oxidation on fatigue cracking behaviour, mechanical properties of oxidised grain boundaries were also investigated by nanoindentation on both the top surface and cross-sections. Selected specimens were sectioned from the centre, mounted into Bakelite resin, and then ground and polished to achieve an appropriate surface quality needed for nanoindentation measurements. Nanoindentation maps of various sizes were performed in order to capture potential changes in mechanical properties across oxidised grain boundaries. Preliminary measurements were carried out in order to optimise the distance between adjacent indents (5 μm) and avoid any interaction effects. Indentation test parameters were kept constant for all the experiments (i.e. loading/unloading time of 10 s, dwell time of 30 s at a maximum load of 5 mN). Drift measurements were carried out for 60 s during the unloading at a load of 10% of the maximum load. The drift rate was calculated from a linear regression of the displacement vs time data and used to correct the nanoindentation data. The Berkovich tip was calibrated before tests by using a standard fused silica sample. Data were corrected for frame compliance before calculation of mechanical properties based on the procedure outlined by Oliver and Pharr [51].

2.5 Oxidation in the pre-loaded LSHR alloy

To investigate the effects of strain (particularly plastic strain) on oxidation of the LSHR alloy, oxidation was conducted on a pre-loaded CG LSHR alloy. The specimen has dimensions of 53 mm × 4 mm × 4 mm with a FIB notch along a twin boundary. The specimen surface was polished and the specimen has been cyclically loaded for 30000 cycles under a sine waveform of 20 Hz at room temperature. The maximum applied strain was of ~ 0.9% based on an FE elastic-plastic simulation. The residual strain distribution in this pre-loaded CG LSHR alloy at room temperature and for 30000 cycles was measured by using the SEM-DIC technique, which is detailed in our recent publication [52]. After pre-loading at room temperature, this specimen was re-polished and then oxidised at 725 ^{o}C for 24 hours, followed by SEM-EDS analyses.

3. Results

3.1 Surface oxidation under cyclic load

Generally, the uninterrupted short crack tests show that the intergranular cracking is dominant features on the fracture surfaces and the interrupted tests show that crack propagation is mainly achieved by coalescence of grain boundary cracks as shown in our previous study [38]. The morphology of the notch root surface ahead of the main crack tip at the end of the interrupted test is presented in Fig. 2. Due to oxidation effects, grain boundaries are visible on the polished notch root surface in both the CG and FG LSHR variants tested at 725 ^{o}C. Bulged oxides and cracks can also be observed, with coarser and more densely distributed bulged grain boundary oxides observed in the FG LSHR variant. The bulged oxides are mostly discernible at the grain boundaries which are oriented *normal* to the tensile stress axis in both CG and FG LSHR variants, and these bulged grain boundary oxides have a faceted morphology as shown in Figs. 2 (b) and (d). However, it is noteworthy that not all of the grain boundaries oriented normal to the tensile stress axis are decorated with bulged oxides, thus indicating the influence of grain orientation and grain boundary character on oxide formation. In addition, bulged oxides are also discerned at the slip bands in the CG LSHR variant as shown in Fig. 2 (a). Although slip bands were frequently detected in the CG LSHR, no apparent slip band initiated cracking was found. The cracks observed at the notch root are predominantly intergranular, indicating grain boundaries are the favoured sites for crack initiation under the investigated conditions.

As shown in Figs. 2 (a) and (c), there are some black replica compounds penetrating into the oxidised grain boundaries due to the grain boundary oxide cracking. These replica compounds are due to the replication process used to monitor crack evolution at the notch root surface. Around the penetrating replica compound, grain boundary oxides can be discerned, especially in the FG LSHR as indicated in Fig. 2 (c), indicating that oxidation leads to crack initiation. Moreover, it is noted that the bulged grain boundary oxides ahead of a crack tip are intact. These intact oxides may also indicate that oxide formation occurs prior to crack initiation and that crack initiation is a consequence of oxide cracking.

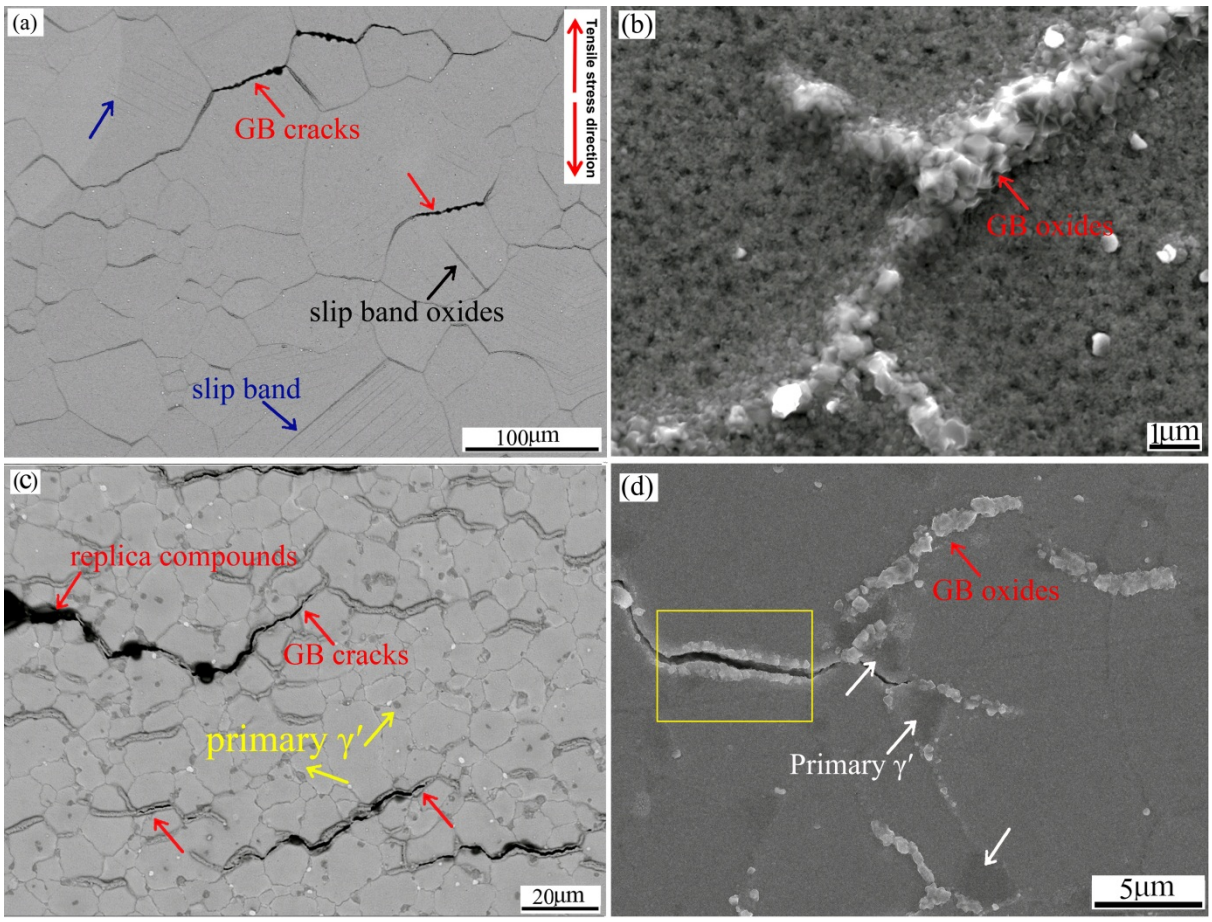

Fig. 2 (a) Morphology of the notch root surface and (b) grain boundary oxide morphology in the CG LSHR variant tested at 725 ^{o}C; (c) morphology of the notch root surface and (d) grain boundary oxide morphology in the FG LSHR variant tested at 725 ^{o}C.

The oxides formed at the notch root surface during the short fatigue crack test were examined by TEM. The TEM lamella was extracted from a region containing grain boundaries with (Fig. 3 (a)) and without (Fig. 4 (a)) bulged oxides. Bulged oxides and oxide intrusions can be observed along the grain boundary and a uniform but much thinner oxide

scale can be observed within the γ grain. As shown in Fig. 3 (c) and the EDS elemental maps, the bulged grain boundary oxides at the surface are Co and Ni oxides with the Co-rich oxides locating on the top of Ni-rich oxides. The oxide intrusion along the grain boundary consists of Cr, Ti and Al oxides with Cr oxides in the centre and Ti/Al oxides at the intrusion/matrix interface. Ni-rich islands which may be recrystallized γ grains are discernible within the oxide intrusion. In addition, γ′ precipitates which are enriched in Ni and depleted in Cr are revealed by EDS mapping as indicated by the bright circular dots in the Ni map and dark circular dots in the Cr map. Formation of Ti and Al oxides is accompanied by γ′ dissolution as indicated by the depletion zone of Al and Ti which is highlighted by the rectangle in Fig. 3 (c). Moreover, as shown in the EDS elemental maps in Fig. 3 (c), an enrichment of Ni, Co and Cr and a depletion of Al and Ti can be discerned ahead of the oxide intrusion tip where no oxygen is detected as highlighted by the red ellipse. This enrichment of Ni, Co, and Cr may provide a prerequisite step in starting a new cycle of non-selective oxidation of Ni and Co and then selective oxidation of Cr/Ti/Al once the grain boundary oxide intrusion cracking occurs.

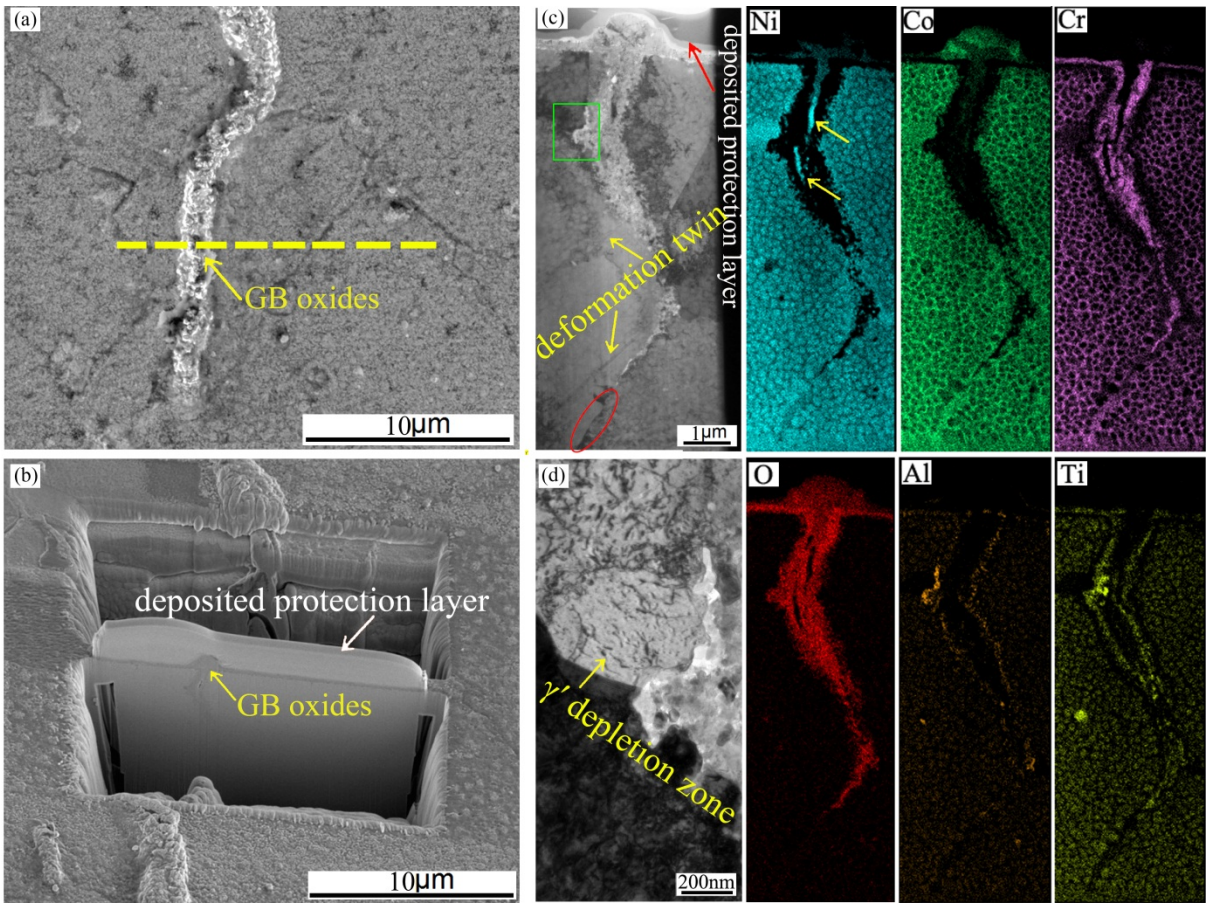

Fig. 3 (a) Area of interest for TEM lamella extraction in the FG LSHR variant tested at 725 ^{o}C. The dashed line indicates the extraction position; (b) TEM lamella in the trench before lift-out procedure; (c) bulged oxides and oxide intrusion along grain boundary and the corresponding EDS elemental maps; and (d) close-up of the γ′ depletion zone highlighted in (c) by the rectangle.

As shown in Fig. 4, little Cr/Ti/Al oxide intrusion can be discerned along the grain boundary without bulged oxides. The thin and uniform oxide scale mainly consists of Cr/Ti/Al oxides along with Ni and Co oxides at the outer surface. A short Al oxide intrusion is seen along the grain boundary and a depletion of Al and Ti nearby the Al oxide intrusion is observed, also indicating the formation of Al and Ti oxides is accompanied by dissolution of γ′ precipitates. In addition, this dissolution of γ′ precipitates is only located at one side of the grain boundary, which indicates the influence of grain orientation on the oxidation process.

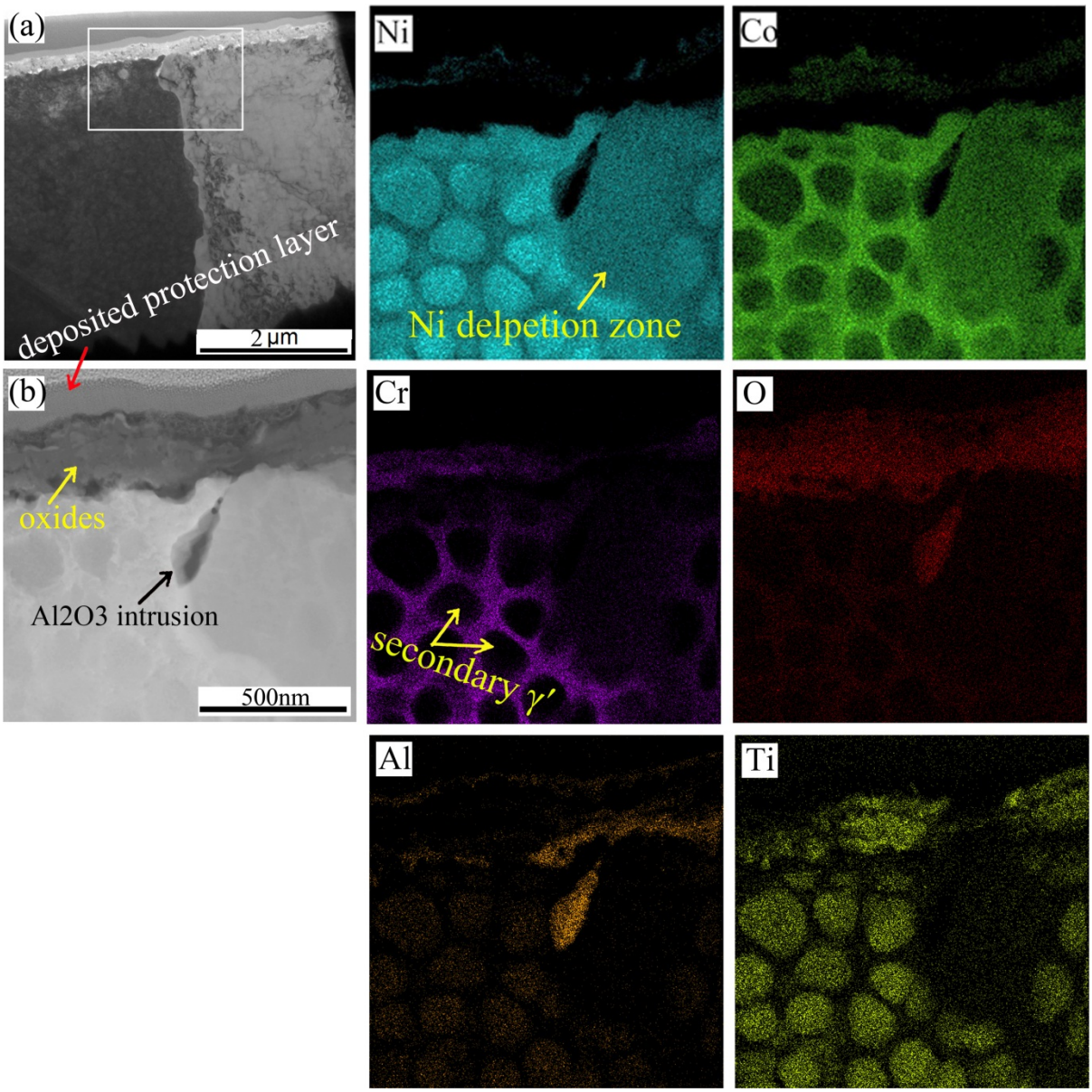

Fig. 4 (a) Morphology of the grain boundary without bulged oxides in the FG LSHR variant tested at 725 ^{o}C; and (b) close-up of the region highlighted in (a) by the rectangle and the corresponding EDS elemental maps.

3.2 Surface oxidation under sustained load

Oxidation under sustained load was investigated by three-point bending at 725 ^{o}C in the MG LSHR. The stress, total strain and plastic strain distribution on the top surface along the longitudinal direction in the plain bend bar specimen based on the FE elastic plastic simulation is shown in Fig. 5 (a). The oxidised surface morphologies after 8 hours under the sustained load at 725 ^{o}C in the five regions highlighted in Fig. 5 (a) are presented in Fig. 5 (b). As shown in Fig. 5, evident grain boundary oxide cracking can be seen in region I close to the

centre. Although it is difficult to quantify the severity of grain boundary oxidation, it clearly shows that the grain boundary oxide density decreases with the decreasing total strain, plastic strain and stress until the grain boundary oxides disappear in a location that is about 4 mm away from the centre. Moreover, it seems that the grain boundary oxide density is more closely related to the plastic strain. The grain boundary oxidation disappears when the plastic strain approaches zero.

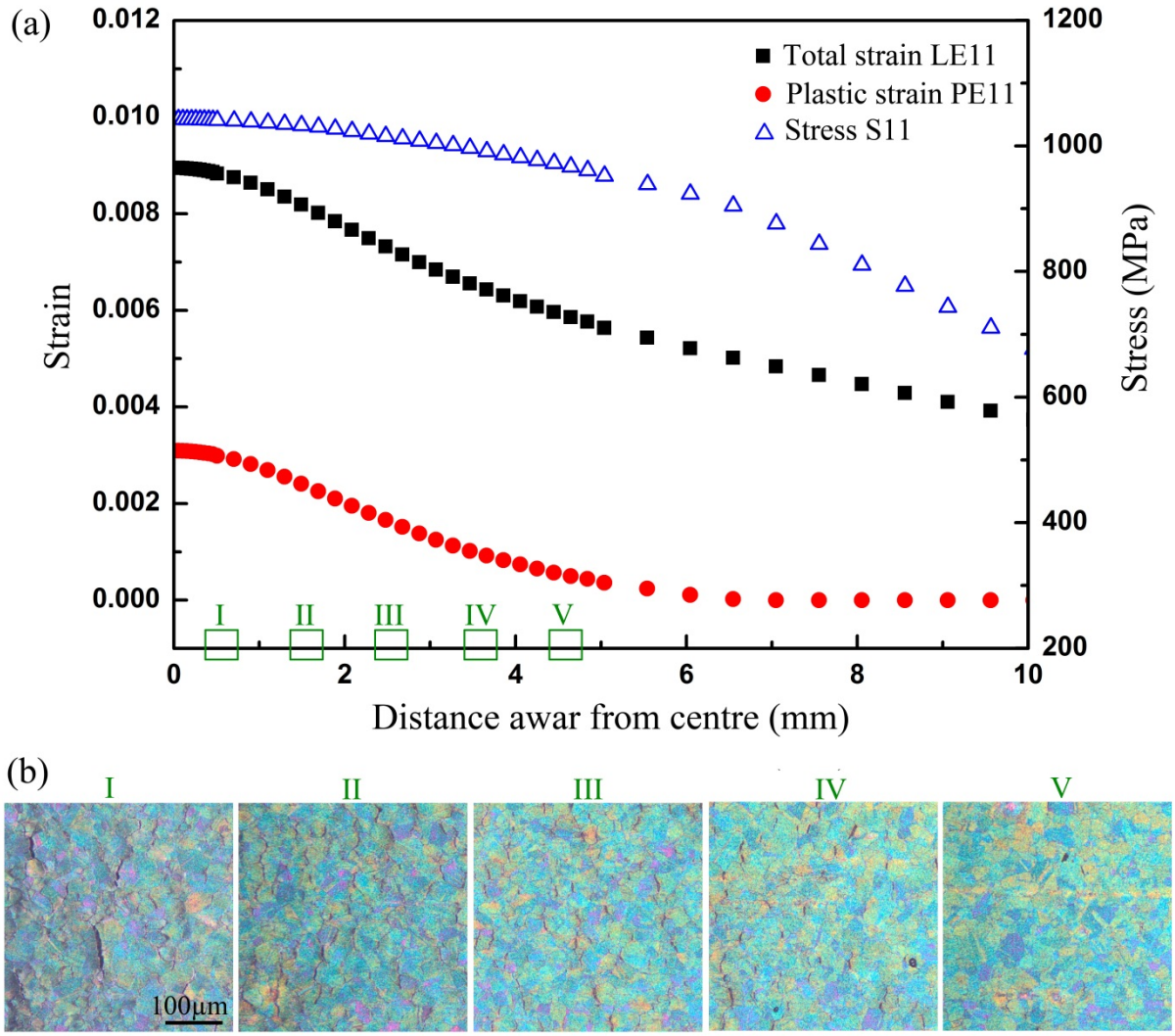

Fig. 5 (a) Total strain, plastic strain and stress distribution at the top surface along the longitudinal direction away from the centre in the MG LSHR specimen based on the FE elastic plastic simulation, and (b) morphology of oxidised surface after 8 hours under the sustained load at 725 ^{o}C in the five regions indicated in (a).

Fig. 6 presents the grain boundary oxides formed under the sustained load at 725 ^{o}C after 1.75 hours and 2.25 hours respectively. Similar to the grain boundary oxidation observed

under the cyclic loads, two types of oxidised grain boundaries are discerned, one is a relatively flat grain boundary, and the other is a grain boundary with bulged oxides. These bulged oxides form at the grain boundaries normally oriented with respect to the tensile stress direction. By comparing Fig. 6 (b) to Fig. 6 (d), it is found new oxides form at a segment of grain boundary in the region highlighted by the red rectangle. Oxide cracking is discerned at 0.5 hour increments, and this oxide cracking can be seen more clearly in the inserted close-up in Fig. 6 (d). Observation of the grain boundary oxide evolution provides evidence of crack initiation due to oxide cracking.

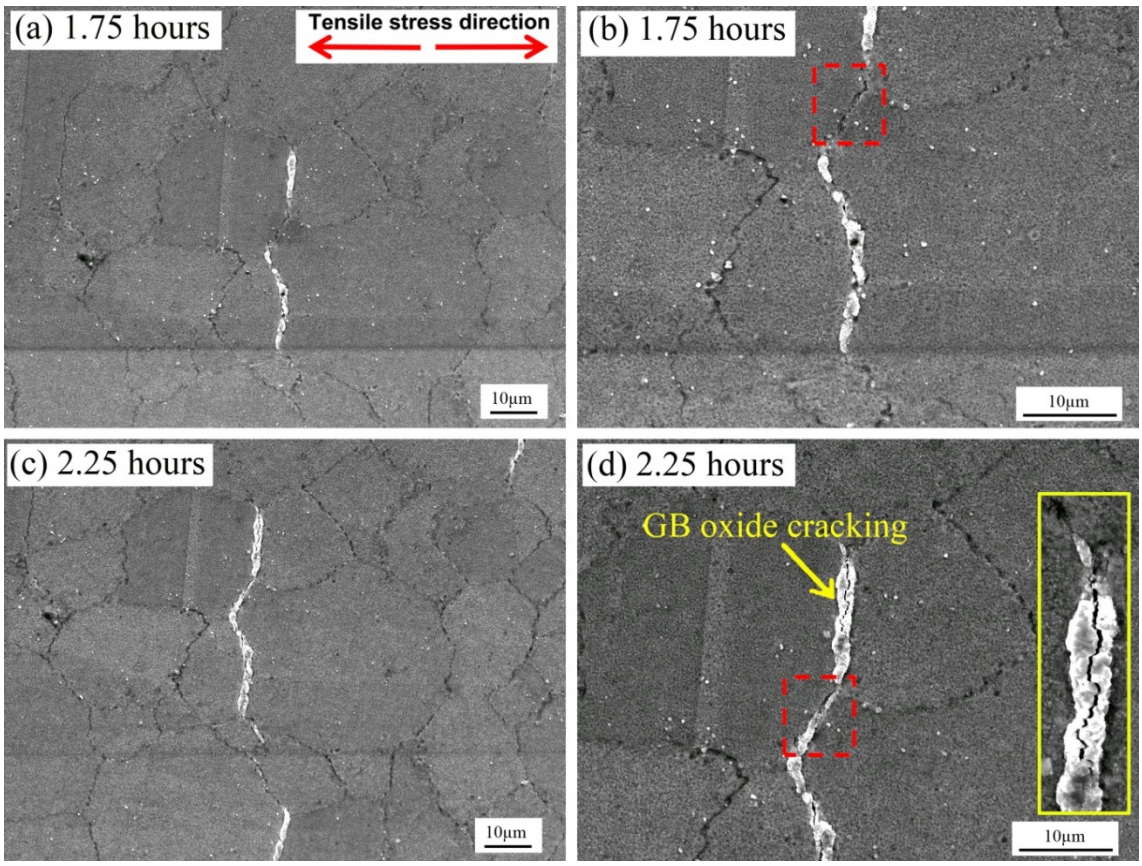

Fig.6 Grain boundary oxidation under sustained load at 725 ^{o}C in the MG LSHR variant: (a) and (b) grain boundary oxidation after 1.75 hours; (c) and (d) grain boundary oxidation after 2.25 hours. The insert close-up in (d) clearly shows the oxide cracking.

Fig. 7 shows the oxide morphology on the top surface after a re-polishing. Due to the mechanical effect of the re-polishing, the layered structure of the grain boundary oxides on the top surface was disclosed. As shown in Fig. 7, the width of the layered grain boundary oxides can be up to 2 μm. EDS examination of the oxide composition shows similar elemental distribution across the grain boundary as shown in Fig. 3, i.e. Ni and Co located at

the centre, Cr enrichment next to Ni and Co, and then the Al and slight Ti enrichment is discerned at the oxide/metal matrix interface. In addition, it seems that the Ni, Co oxides are much coarser than the Cr/Al/Ti oxides. The size of Al and Ti oxides seem to be comparable with secondary γ′.

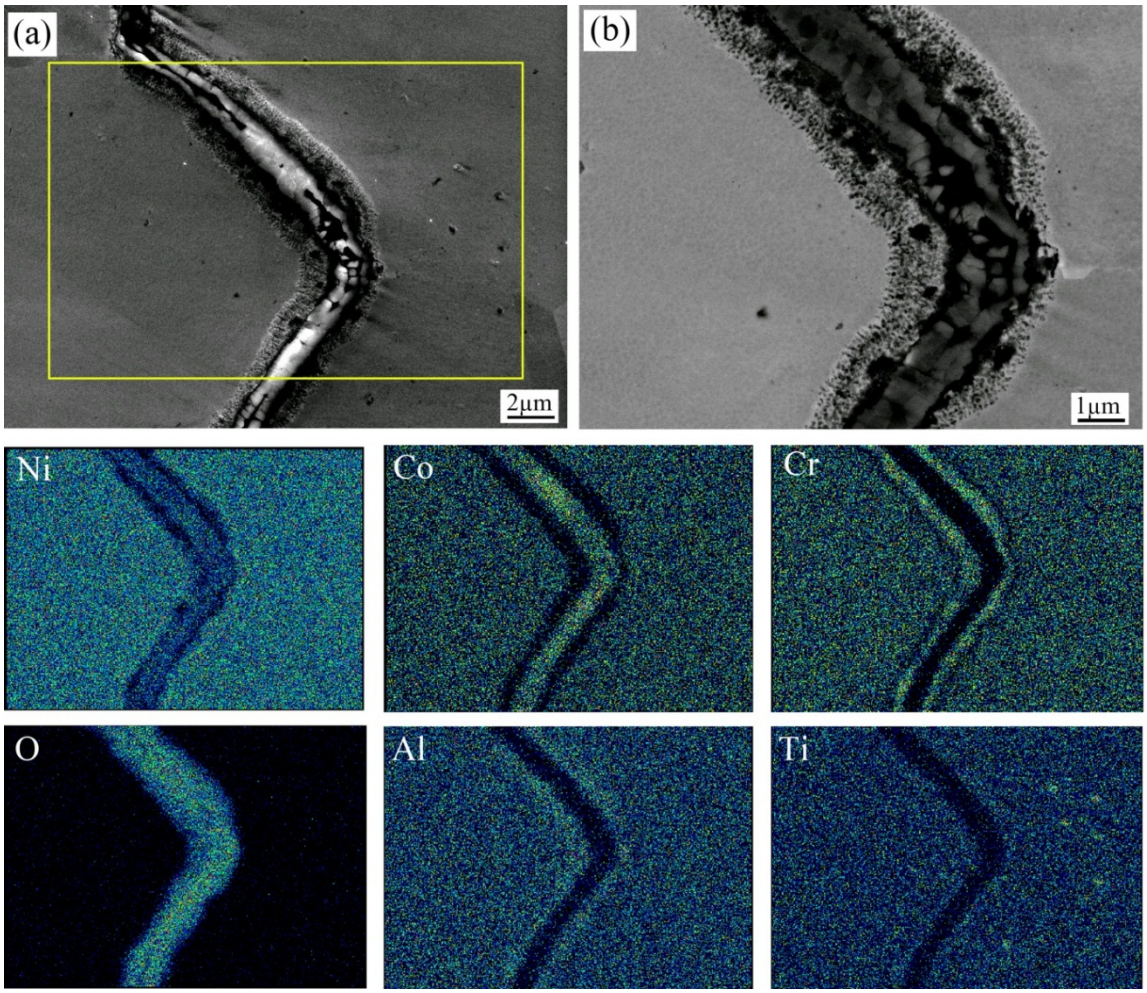

Fig. 7 (a) Secondary electron image and (b) backscatter electron image of grain boundary oxides after re-polishing the oxidised surface in the MG LSHR variant, and the corresponding elemental maps of the region highlighted in (a).

To better understand the effects of grain boundary oxidation on crack initiation, mechanical properties of regions surrounding oxidised grain boundaries were locally assessed by nanoindentation. Fig. 8 (a) shows the morphology of an oxide intrusion (with a very similar layered structure to that observed on the top surface (Fig. 7)) extending tens of microns below the top surface. In order to capture changes in mechanical properties, nanoindentation maps were centred over oxidised grain boundaries (see an example in Fig. 8 (a)). Fig. 8 (b) shows the close-up of some indents performed across an oxide intrusion and in

different grains. Due to the anisotropic properties of grains with different crystallographic orientations, indents of different sizes can be observed in different grains (i.e. the central-bottom indent in Fig. 8 (b) exhibits a reduced projected area compared to the side indents). Due to their brittle nature, occasionally oxides formed along grain boundaries came off during the mechanical polishing process, as it is the case shown in Fig. 8 (b). However, oxides were still present in the main crack (Fig. 8 (a)) after mechanical polishing. Fig. 8 (c) shows an approximate crack morphology superimposed to the hardness map. A clear hardening effect around and at the oxidised grain boundary is observed. In particular, three regions in terms of mechanical properties can be identified around the oxide intrusion: (i) surrounding metallic structure (20 – 30 μm away from the oxide intrusion) with a hardness of ~ 3 – 5 GPa, (ii) metallic region below the surface and close to the oxidised grain boundary (5 – 10 μm away from the oxide intrusion) exhibiting a hardness of ~ 5 – 7 GPa, and (iii) oxide intrusion exhibiting a peak hardness of ~ 9 GPa. In regions unaffected by compositional variations (i.e. regions related to point (i) and (ii) above), changes in hardness were caused by different crystallographic orientations between adjacent grains, as suggested by the contrast in the micrograph reported in Fig. 8 (a) and 8 (b), as well as by the formation of structural defects (e.g. slip bands) following mechanical tests.

The corresponding reduced modulus map is presented in Fig. 8 (d), where beside some singularities attributed to indents performed on oxides, two main regions with reduced modulus above and below ~ 200 GPa were identified. These differences are attributed to the synergetic effect of different crystallographic orientations and structural defects caused by local deformations near the grain boundary.

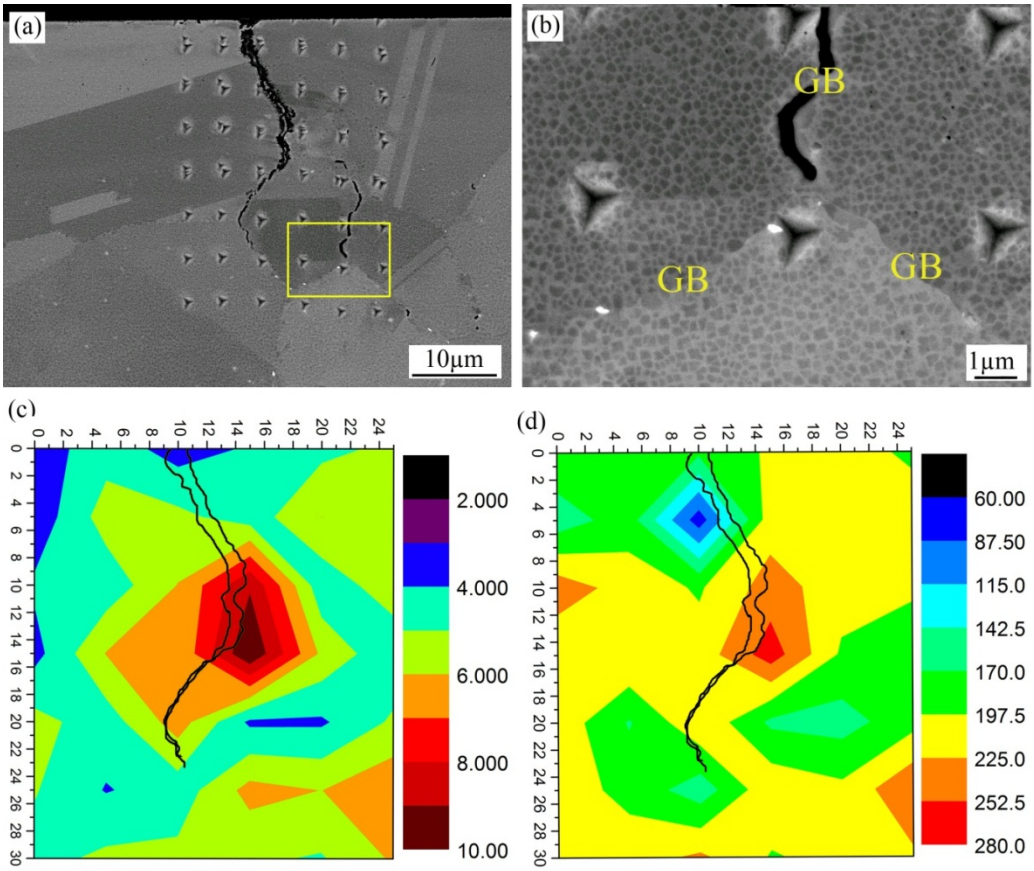

Fig. 8 – (a) Morphology of an oxidised grain boundary and indentation map in cross-section for the MG LSHR, (b) close-up of the region highlighted by the rectangle in (a), (c) hardness map and (d) reduced elastic modulus map across the oxidised grain boundary. An approximate crack morphology was superimposed on the maps in (c) and (d) to allow better interpretation of the maps around the crack. Mechanical properties were determined based on the first and larger indentation map shown in (a) – a superimposed smaller indentation map was also performed afterwards for a different purpose.

3.3 Surface oxidation in the pre-loaded LSHR alloy

Fig. 9 shows the surface oxidation in the pre-loaded CG LSHR variant at 725 ^{o}C for 24 hours. The CG LSHR specimen has been cyclically loaded for 30000 cycles before oxidation; in Fig. 9 (a) a few cracks are highlighted by arrows. The residual maximum shear strain distribution is measured by SEM-DIC and is presented in Fig. 9 (b). Details of the strain measurement procedure using SEM-DIC can be found in our recent publication [52]. As shown in Fig. 9 (b), the strain distribution displays a pattern of strain bands and intensive deformation can be seen around the crack. Fig. 9 (c) shows the oxidation occurring at 725 ^{o}C after 24 hours. It is found that the bulged oxides mainly form in the intensively deformed regions which are usually associated with cracks and crack tips. Figs. 9 (d) - (g) show close-

ups of the oxides around the cracks, at the crack tips and/or slip bands. As shown in Fig. 9 (d), no apparent oxide formation is found around the crack initiated from the twin boundary (where the deformation is highly concentrated). Conversely, a slip/strain band which is slightly away from and parallel to the twin boundary shows bulged oxide formation as shown in Fig. 9 (e). Based on the oxidation in the pre-loaded LSHR alloy, there appear to be a threshold strain value for oxidation to occur, and oxidation preferentially develops in these intensively deformed regions.

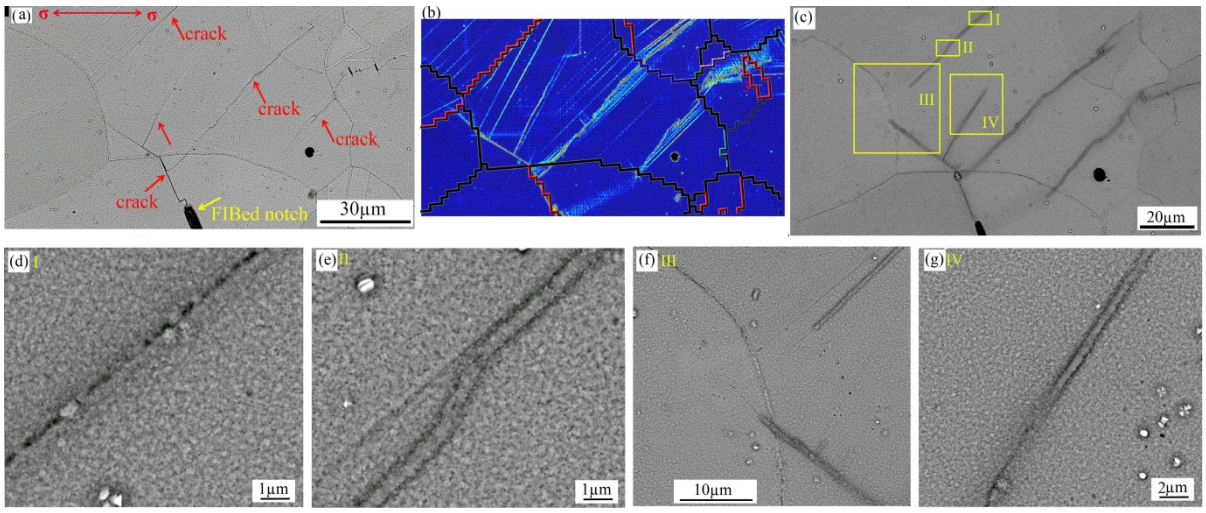

Fig. 9 Oxidation in the pre-loaded CG LSHR variant at 725 °C for 24 hours: (a) morphology in the area of interest after pre-loading; (b) residual maximum shear strain distribution in the area of interest after pre-loading. Grain boundaries obtained by EBSD are overlaid on the strain map; (c) morphology in the area of interest after oxidation; (d), (e), (f) and (g) close-ups of the oxidation in the regions I, II, III and IV indicated in (c) respectively.

3.4 Oxidation at the fatigue crack tip

Oxidation at the crack tip has been evaluated in both short fatigue crack tests and long fatigue crack growth tests. Fig. 10 presents the crack paths in the CG and FG LSHR alloy variants from the short crack tests after sectioning the tested specimens. The measured crack length *a* from the notch root to the crack tip and the corresponding ΔK at the crack tip are also labelled in Fig. 10. The calculation of ΔK was based on an embedded semi-elliptic crack in a plate subjected to bending conditions as illustrated in a review by Scott and Thorpe [53] and was detailed in [13, 50]. As shown in Fig. 10, apart from the CG LSHR tested at 650 °C, the crack paths are intergranular in other tests, even though the ΔK at the crack tip is quite high. Such high ΔK levels are usually associated with fast unstable crack propagation. In the

CG LSHR variant tested at 650 °C, there is a transition from intergranular to transgranular crack propagation at a ΔK of ~66 MPa√m.

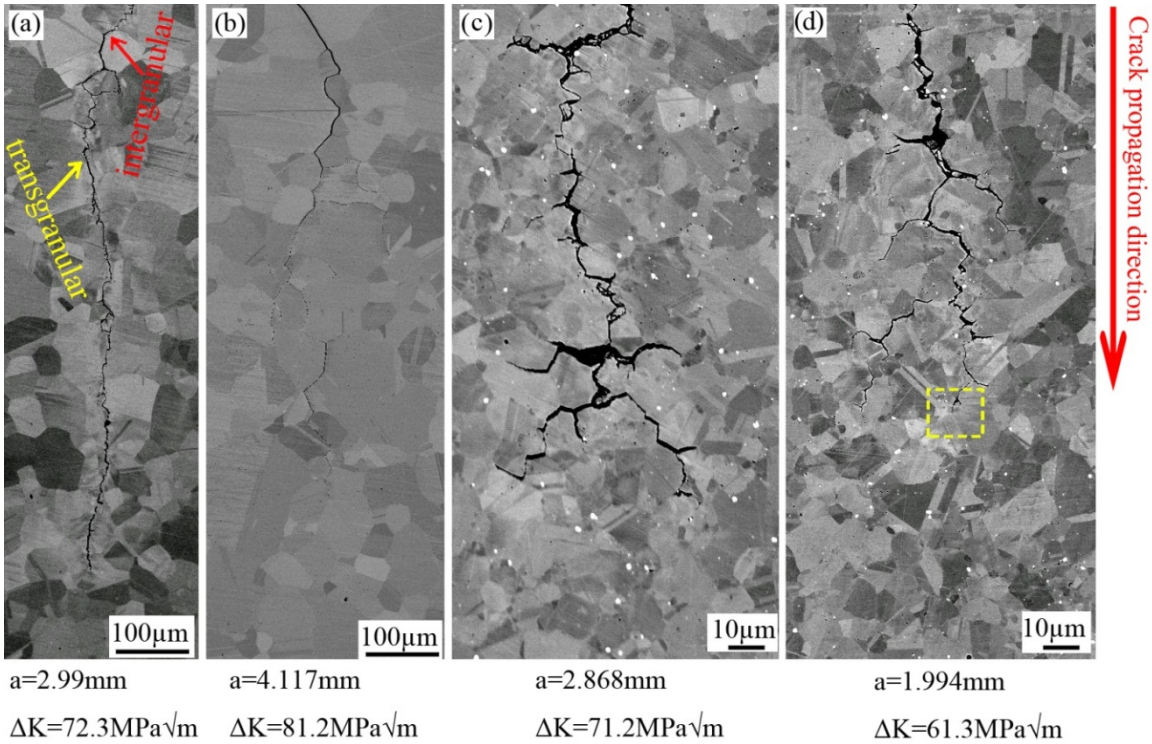

Fig. 10 Crack path in the bulk materials: (a) CG LSHR, 650 °C; (b) CG LSHR, 725 °C; (c) FG LSHR, 650 °C; and (d) FG LSHR, 725 °C. The total crack length and the ΔK at the crack tip are labelled in the figure. The rectangle in (d) indicates the in-plane TEM lamella extraction site.

The oxidation at the crack tip was examined by TEM-EDS. An in-plane TEM lamella (parallel to the crack propagation direction) was extracted at the crack tip (region highlighted in Fig. 10 (d)) in the FG LSHR variant tested at 725 °C. Fig. 11 shows the crack tip morphology and the EDS elemental maps around the crack tip. It can be seen that this crack tip is stopped at a primary γ′. A close-up of the crack tip (Fig. 11 (b)) shows an oxide layer along the crack wake and an oxide intrusion ahead of the crack tip at the γ/γ′ interface. Although it is arguable that the oxide layer at the crack wake may be formed before or after the cracking of the grain boundary, the uncracked oxide intrusion ahead of the crack tip supports the assumption of oxide cracking leading to crack propagation. As shown in the elemental maps, the layered oxide structure is not evident. It seems that the oxide intrusion mainly consists of Co and Cr oxides. Meanwhile, the depletion of Ni, Al and Ti in the primary γ′ indicates that the oxidation occurs at the γ/γ′ interface and towards the primary γ′.

In addition, an Al oxide is seen within the primary γ′ and a Ti-rich precipitate is located at the γ/γ′ interface. It seems that these Al oxide and Ti-rich precipitates are inherited from the manufacturing process. The absence of any Al and Ti oxide layer is probably related to the dynamic advancing crack tip progressing at high speed at this high ΔK level (~ 60 MPa√m), which fails to provide enough time to form dense Ni/Co and Cr oxide layers at the crack tip before crack advance occurs and hence not to produce low enough oxygen partial pressure at the oxide/metal interface for Al and Ti oxide formation.

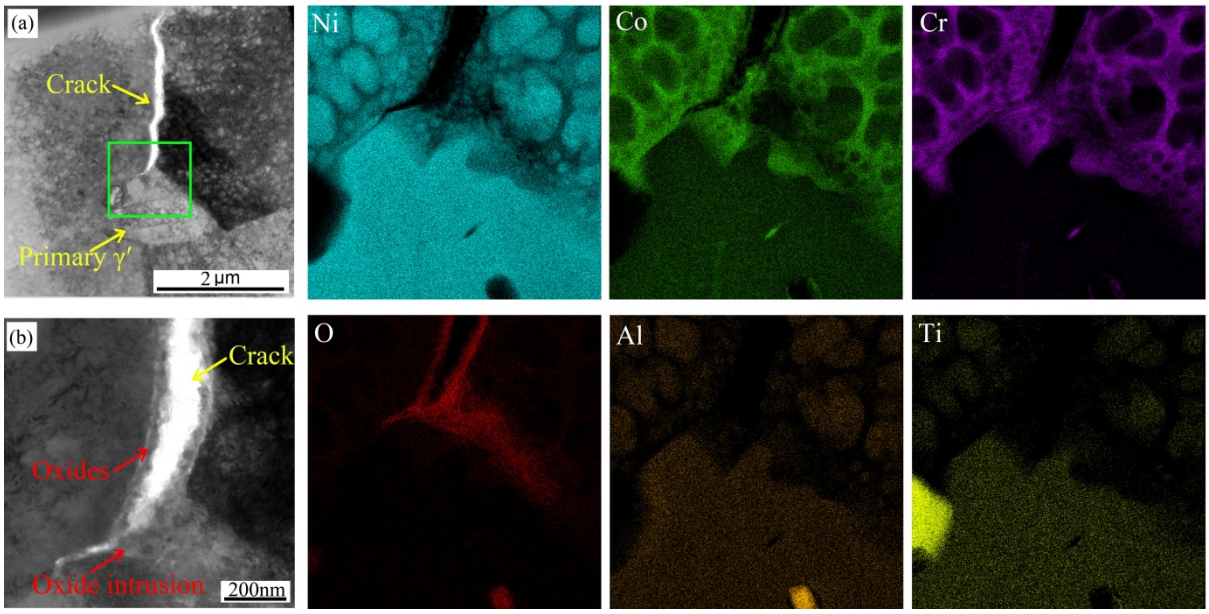

Fig. 11 (a) Morphology of the crack tip in the FG LSHR variant at 725 °C and the corresponding EDS elemental maps in the region highlighted by the rectangle; and (b) close-up of the crack tip.

In the short fatigue crack tests, it is difficult to monitor the crack propagation into the bulk material, making it difficult to assess the oxidation at the crack tip at different ΔK levels and different crack propagation rates. To systematically assess oxidation at the crack tip, long FCG tests were conducted on MG LSHR variant at 725 °C under 1-300-1-1 and 1-90-1-1 loading waveform. $^{18}O_2$ was introduced into the test chamber when the ΔK at the crack tip reached ~16 MPa√m and ~25 MPa√m in the 1-300-1-1 tests and ~40 MPa√m in the 1-90-1-1 test respectively. The obtained crack growth rates are shown in Fig. 12 (a). The crack growth rates were 30 μm/cycle, 150 μm/cycle and 252 μm/cycle respectively in the three investigated scenarios before stopping the test. Intergranular crack paths can be clearly seen in all scenarios after sectioning the tested specimen from the centre as shown in Figs. 12 (b), (d) and (f). In the specimens which were stopped at ΔKs of ~16 MPa√m and ~25 MPa√m in

the 1-300-1-1 tests, significant enrichment of $^{18}O^-$ is found at the crack tips as shown in Figs. 12 (c) and (e), especially at the crack tip at a ΔK of ~16 MPa√m with the much slower crack propagation rate. This significant enrichment of $^{18}O^-$ indicates the occurrence of significant GB oxidation during the few loading cycles applied after the interruption to introduce the gas tracer. With a crack growth rate (ΔK level) increase and the reduced dwell time at the maximum load, oxidation at the crack tip is observed to diminish. As shown in Figs. 12 (f) and (g), although an intergranular crack path is clearly seen at the crack tip at a ΔK of ~40 MPa√m in the 1-90-1-1 test, $^{18}O^-$ is not detected at the crack tip, but only limited $^{16}O^-$ is discerned at the crack tip as shown in Fig. 12 (g).

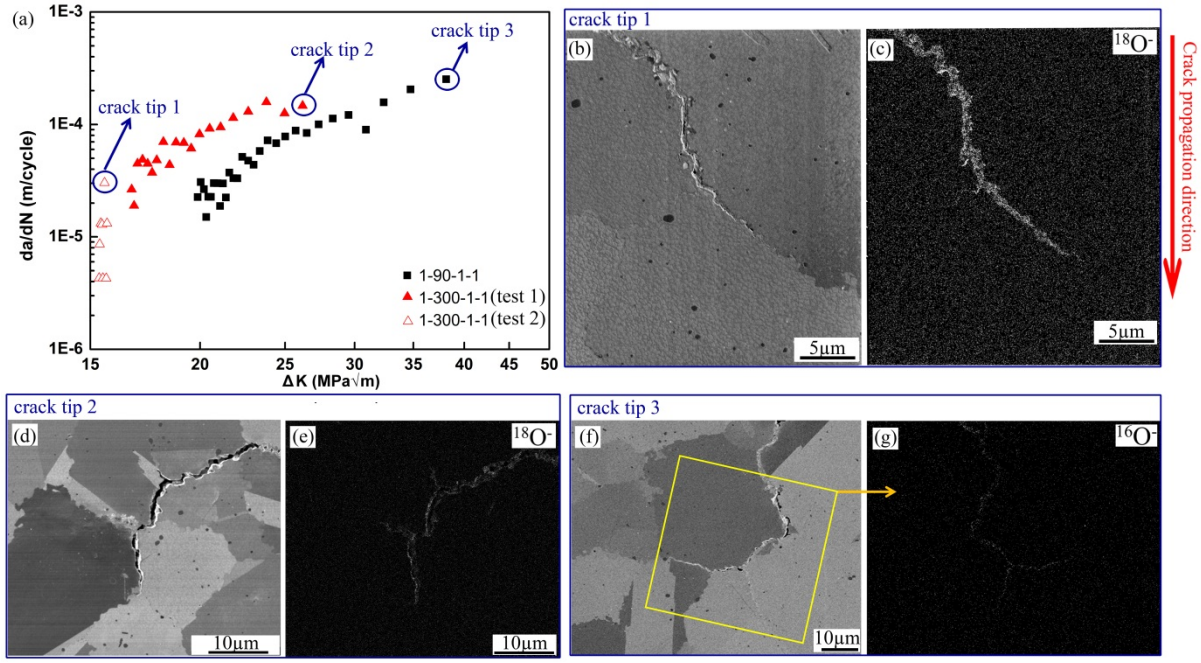

Fig. 12 Oxidation and oxygen distribution at the propagating crack tips: (a) crack propagation rates; (b) crack tip morphology and (c) $^{18}O^-$ distribution at the crack tip at a ΔK of ~16 MPa√m under the loading waveform of 1-300-1-1; (d) crack tip morphology and (e) $^{18}O^-$ distribution at the crack tip at a ΔK of ~25 MPa√m under the loading waveform of 1-300-1-1; (f) crack tip morphology and (g) $^{16}O^-$ distribution at the crack tip at a ΔK of ~40 MPa√m under the loading waveform of 1-90-1-1.

4. Discussion

4.1 Mechanisms of stress/strain-assisted (GB) oxidation

The oxides that form under either cyclic loads or sustained loads exhibit a layered structure, with the outermost Co, Ni oxide layer, intermediate Cr_2O_3 oxide layer and an inner Al, Ti

oxide layer at the oxide/metal interface. This layered oxide structure is similar to that observed at the crack tips in disc alloy U720Li and RR1000 under sustained load [15, 20, 34]. The net oxidation products are a function of the investigated alloys, temperature, oxygen partial pressure and applied strain/stress [7, 9, 13, 24, 26, 38, 43]. Generally, fine microstructure, high temperature, high oxygen partial pressure and high applied strain are associated with severe grain boundary and γ/γ′ interface oxidation as indicated in the short fatigue crack tests in this study (Fig. 2).

Although there are several models and simulations based on the assumption of stress assisted diffusion/oxidation, it seems that the oxidation processes are more closely related to the plastic *strain*. As shown in the sustained load oxidation test in Fig. 5, grain boundary oxidation diminishes as plastic strain decreases and disappears when plastic strain approaches zero. This effect of plastic strain on the oxidation process can be further verified by the preferential oxidation in the regions/strain bands with intensive deformation as shown in Fig. 9 in the pre-loaded CG LSHR variant. It is widely accepted that the rate-controlling step of oxidation in Ni-based superalloys is the diffusion of oxide forming elements [28, 42, 54]. In the case of this study, the oxidation, particularly the *grain boundary* oxidation, is mainly determined by the outward diffusion of Ni^{2+} and Co^{2+} and inward diffusion of O^{2-}, which is closely related to short-circuit diffusion paths such as grain boundaries and dislocations [42]. Generally, higher plastic strain is usually associated with higher dislocation density. As a result, fast oxide-forming element diffusion and consequently fast oxidation occurs. A similar effect of plastic strain on accelerated element diffusion process can also be found in enhanced stainless steel corrosion [44]. Compared to plastic strain, elastic strain has a limited contribution to the defect density in the loaded materials, and thereby it is expected that the accelerated diffusion caused by elastic strain is insignificant. However, the stress applied in the elastic regime can help to accommodate the volume expansion during oxide formation, which is believed to accelerate oxidation to some extent as analysed in a few analytical models [35, 54, 55]. In addition, it also should be noted that the localised growth stress and strain due to oxide formation and the oxidised grain boundaries may also alter the local diffusion process and exerts an influence on the local oxidation process.

Macroscopically it is clear that the global applied stress (and in continuum assumptions therefore also the strain) has an influence on the oxidation process. Microscopically, it seems that the oxidation process is more closely related to the accumulated *local* strain/stress which is associated with grain mis-orientation and grain boundary character [21, 29]. In this study,

significant discrepancy of oxidation between different grain boundaries was observed (Fig. 2). As reported in a recent study, the bulged Ni/Co-rich oxides along with Ti/Cr/Al oxide intrusion preferentially form at the boundaries between high and low Schmid factor (SF) grains that are oriented normal to the tensile stress axis [21]. The grain boundaries or other interfaces with accumulated local strain (or stress concentration) can either provide the stored strain energy to overcome the barrier to oxide nucleation or provide short-circuit diffusion paths (e.g. dislocations) to facilitate oxide-forming element diffusion. It is therefore expected that more significant oxidation occurs in these regions. Further study of stress/strain assisted GB oxidation would require measurement of stress/strain distribution at the grain level at elevated temperatures. This is now under consideration by using SEM-DIC technique in future work.

4.2 Role of oxidation in fatigue cracking

Based on the observation of the notch roots and fracture surfaces, cracks predominantly initiate along grain boundaries in both CG and FG LSHR due to oxidation in the investigated conditions, even though crack initiation from slip bands, subsurface pores and inclusions has also been observed at elevated temperatures in the LSHR alloy [22]. This difference in crack initiation is probably caused by the relatively high strain achieved at the notch root in this study which accelerates grain boundary oxidation. In addition, the grain boundary oxide cracking under the sustained load (Fig. 6) further supports crack initiation due to GB oxidation. The oxide cracking under static/cyclic loading is due to its hard and brittle nature as indicated by nanoindentation data and therefore its apparent low fracture toughness.

In terms of fatigue crack propagation, enhanced fatigue crack propagation associated with intergranular cracking is widely observed in PM Ni-based superalloys under dwell-fatigue conditions at elevated temperatures in aggressive environments [7, 9, 13, 15, 16]. This enhanced intergranular crack propagation is closely related to fine microstructures of the Ni-based superalloys, high temperatures, high oxygen partial pressure and a long dwell time at the peak load [7-9, 13, 15, 16, 24]. As shown in this study, and also in a previous work [9], intergranular fracture is found in the FG LSHR variant at 650 and 725 ^{o}C and in the CG LSHR variant at 725 ^{o}C under a 1-1-1-1 loading waveform. But there is a transition from intergranular to transgranular crack propagation in the CG LSHR at 650 ^{o}C either in the short fatigue crack test as shown in Fig. 10 or in the long fatigue crack growth test as shown in [9]. This transition from intergranular to transgranular crack propagation is believed to be a consequence of the competing effects between oxygen-related damage (i.e. stress/strain-

assisted grain boundary oxidation and dynamic embrittlement) and mechanical damage, which further depends on the accumulated strain/stress at the crack tip, the crack propagation rate and the delivery rate of oxygen to the crack tip.

Fig. 13 schematically illustrates the contribution of stress/strain assisted grain boundary oxidation, dynamic embrittlement and mechanical damage to fatigue crack propagation at various stages after crack initiation. In the short fatigue test, immediately after crack initiation, the mechanical driving force for crack propagation is relatively low. Oxidation therefore has enough time to occur ahead of the crack tip due to the relatively low crack propagation rate, and this oxidation process is accelerated by the high temperature and high local strain, resulting in intergranular crack propagation. This increased contribution of oxidation to fatigue crack propagation just after immediate crack initiation can be seen in Udimet 720Li. A transition from transgranular crack initiation to intergranular crack propagation has been observed in Udimet 720Li as shown in Fig. 13 (b), due to the relatively low initial strain and subsequent increase in local strain ahead of the crack tip as crack propagates (which gives rise to more significant oxidation effect ahead of the crack tip) [10].

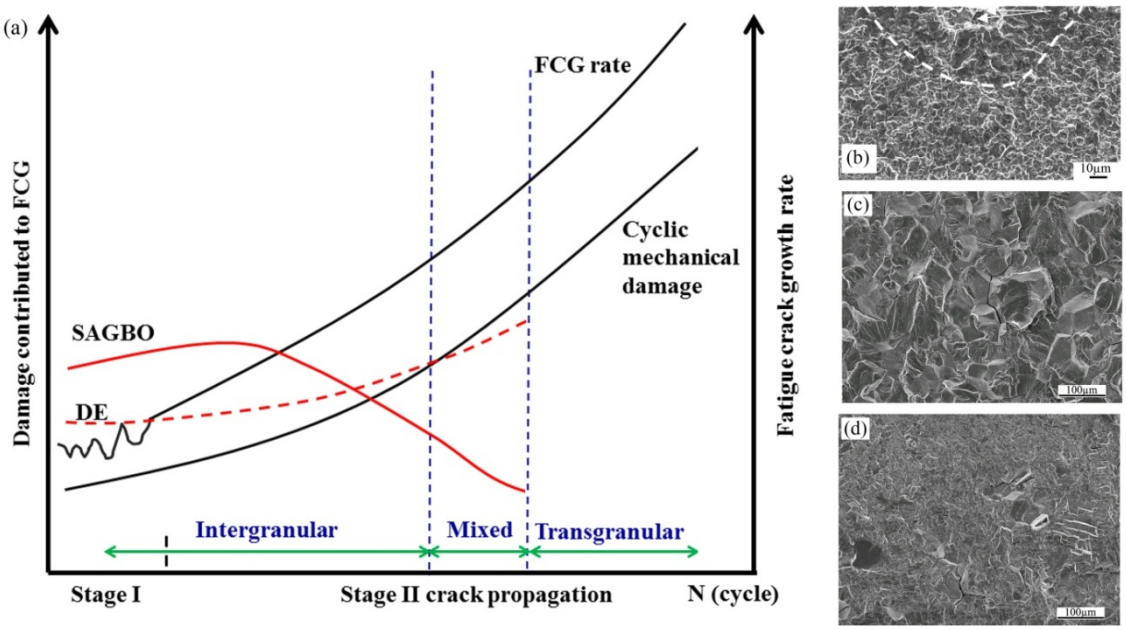

Fig. 13 (a) Schematic diagram showing the contribution of SAGBO, DE and mechanical damage to FCG at various stages of crack propagation, (b) example of transition of transgranular to intergranular crack propagation in U720Li in the stage I crack propagation [10], (c) and (d) example of transition of predominantly intergranular crack propagation at ΔK of 20 MPa√m to transgranular crack propagation at ΔK of 40 MPa√m in the CG LSHR alloy variant [9].

As a crack propagates into Stage II, on the one hand, the increased local stress and strain at the crack tip can accelerate oxidation process; on the other hand, the increased crack propagation rate reduces the available oxidation time in a loading cycle. In addition, the delivery of oxygen to the propagating crack tip is hindered to some extent due to the tortuous nature of the crack path and the crack closure effect. This is supported by the results reported in [13], where significant oxidation was found on the polished side surface of SENB specimen of LSHR alloy, but no evident oxides were observed at the fast propagating crack tip. Under the dwell-fatigue conditions, the oxides that form during the dwell period may build up at the crack tip or may be subject to a dynamic oxide formation-cracking cycle depending on the ΔK level at the crack tip, as illustrated in Li's study [15]. However, in the scenario of no oxide cracking during the dwell period at the low ΔK level or in the scenario of dynamic oxide formation and cracking during the dwell period at the relatively high ΔK level, the contribution of oxidation to crack propagation increases with crack propagation until a transitional fatigue crack propagation rate is reached. Beyond this transitional fatigue crack propagation rate, there is insufficient time at the crack tip for evident oxidation to occur, and the oxidation effect diminishes as shown in Fig. 12, where no apparent enrichment of $^{18}O^{-}$ was detected at the crack tip at a relatively high ΔK level with high crack propagation rate. With further increases in fatigue crack propagation rate, then the mechanisms contributing to intergranular crack propagation may be dominated by dynamic embrittlement.

As the dynamic embrittlement mechanism is mainly linked to stress-assisted oxygen diffusion along the grain boundary within the nanometre scale [18, 19], it is expected that the contribution of dynamic embrittlement to fatigue crack propagation is closely related to local stress/strain acting on the grain boundaries at the crack tip and is increased with the applied stress/strain at the crack tip as indicated in the analytical model proposed by Bika [40], where only one-dimensional diffusion of oxygen along the grain boundary is considered. At the higher ΔK level, it is feasible for repeated processes of dynamic embrittlement-grain boundary cracking to occur, resulting in overall rapid crack growth. With further increases in crack propagation rate, the mechanical damage which is mainly determined by the far field applied stress, the crack length and the strength of the investigated material may then start to outstrip the oxygen-related damage ahead of the crack tip, giving rise to transgranular crack propagation. This is supported by our observations of how the predominantly intergranular crack propagation at ΔK of 20 MPa√m converts to transgranular crack propagation at ΔK of

40 MPa√m at 650 ^{o}C under a 1-1-1-1 load waveform in the CG LSHR alloy variant as shown in Figs. 13 (c), (d) and [9].

5. Conclusions

The role of oxygen in fatigue crack initiation and propagation in PM Ni-based superalloy LSHR at elevated temperatures was evaluated by a range of testing and characterisation procedures for specimens tested by three-point bending in U-notch specimens and SENB specimens. Sustained load oxidation and oxidation in the pre-loaded LSHR were used to study the evolution of GB oxides and the effect of residual plastic strain on the oxidation process. Based on the aforementioned results and discussion, the following conclusions can be made:

(1) Oxides forming under either cyclic load or static load consist of layered structures at the surface, i.e. an outermost Ni/Co oxide layer, an inner Al/Ti oxide layer at the oxide/metal interface, and an intermediate Cr oxide layer in between. At the fast propagating crack tip, only Co and Cr oxides are observed. The grain boundary oxidation is promoted by fine microstructures and higher temperatures.

(2) Macroscopically, formation of these layered oxides is more closely related to the global plastic strain. The grain boundary oxidation diminishes as plastic strain decreases until bulged Ni/Co grain boundary oxides disappear when the plastic strain approaches to zero. Microscopically, formation of the bulged grain boundary Ni/Co oxides and Cr/Ti/Al oxide intrusion is closely related to the strain localisation which is associated with grain orientation and applied stress. The formation of Ti and Al oxides are accompanied by dissolution of γ'.

(3) For the LSHR alloy, grain boundary oxide cracking is the principal mechanism for crack initiation at elevated temperatures in air under dwell-fatigue conditions when plastic strain levels are achieved during the test.

(4) In the early crack propagation regimes, oxidation makes a dominant contribution to these processes. As the crack propagation rate increases, the contribution of oxidation diminishes, and the mechanism for oxygen enhanced fatigue crack propagation may be overtaken by dynamic embrittlement. With further increase of fatigue crack propagation rate, the mechanical damage may outstrip the oxygen-related damage, resulting in a transition from intergranular to transgranular crack propagation. Fine microstructure, high temperature and

high oxygen partial pressure can enhance the oxygen-related damage, and thereby delay the transition of intergranular-transgranular crack propagation to some extent.

Dataset statement

The raw data presented in this paper is available on request from the Dr. Rong Jiang at Nanjing University of Aeronautics and Astronautics (Email: rjiang@nuaa.edu.cn).

Acknowledgements

Thanks are due to the EPSRC (Grant EP/K027271/1) in the UK for funding for this work, and to NASA in the US for the supply of the LSHR alloy. The authors are grateful to Dr. Michael Ward and Dr. Z. Aslam at the University of Leeds for their help in FIB-TEM lamella preparation and TEM-EDS examination of grain boundary oxides. The authors also would like to thank Prof. Liguo Zhao at Loughborough University, Dr. Mark Hardy at Rolls-Royce, Dr. Gordon McColvin at GE Power, Dr. Matthew Lunt at Defence Science and Technology Laboratory, Prof. Scott Lockyer and Dr. Katherine Soady at Uniper Technologies Ltd for useful discussions. RJ would like to thank Nanjing University of Aeronautics and Astronautics (reference number: 1002-YAH18002) for financial support. MC acknowledges Innovate UK (reference number: 113072) for financial support.

Reference

[1] R.C. Reed, The Superalloys: fundamentals and applications, Cambridge University Press, 2006.
[2] T.M. Pollock, S. Tin, Nickel-Based superalloys for advanced turbine engines: chemistry, microstructure and properties, Journal of Propulsion and Power, 22 (2006) 361-374.
[3] J.Y. Guedou, J.C. Lautridou, Y. Honnorat, N18, Powder metallurgy superalloy for disks: Development and applications, Journal of Materials Engineering and Performance, 2 (1993) 551-556.
[4] P.M. Mignanelli, N.G. Jones, E.J. Pickering, O.M.D.M. Messé, C.M.F. Rae, M.C. Hardy, H.J. Stone, Gamma-gamma prime-gamma double prime dual-superlattice superalloys, Scripta Materialia, 136 (2017) 136-140.
[5] Q.Y. Yu, Z.H. Yao, J.X. Dong, Deformation and recrystallization behavior of a coarse-grain, nickel-base superalloy Udimet720Li ingot material, Materials Characterization, 107 (2015) 398-410.
[6] E. Andrieu, R. Molins, H. Ghonem, A. Pineau, Intergranular crack tip oxidation mechanism in a nickel-based superalloy, Materials Science and Engineering: A, 154 (1992) 21-28.
[7] R. Molins, G. Hochstetter, J.C. Chassaigne, E. Andrieu, Oxidation effects on the fatigue crack growth behaviour of alloy 718 at high temperature, Acta Materialia, 45 (1997) 663-674.
[8] D.G. Leo Prakash, M.J. Walsh, D. Maclachlan, A.M. Korsunsky, Crack growth micro-mechanisms in the IN718 alloy under the combined influence of fatigue, creep and oxidation, International Journal of Fatigue, 31 (2009) 1966-1977.
[9] R. Jiang, S. Everitt, M. Lewandowski, N. Gao, P.A.S. Reed, Grain size effects in a Ni-based turbine disc alloy in the time and cycle dependent crack growth regimes, International Journal of Fatigue, 62 (2014) 217-227.
[10] H.T. Pang, P.A.S. Reed, Microstructure effects on high temperature fatigue crack initiation and short crack growth in turbine disc nickel-base superalloy Udimet 720Li, Materials Science and Engineering: A, 448 (2007) 67-79.

[11] J. Telesman, T. P. Gabb, A. Garg, P. Bonacuse, J. Gayda, Effect of microstructure on time dependent fatigue crack growth behavior in a P/M turbine disk alloy. In: R.C. Reed, K. A. Green, P. Caron, T. P. Gabb, M. G. Fahrmann, E. S. Huron, S. A. Woodard, editors. Superalloys 2008. Warrendale (PA): The Minerals, Metals & Materials Society; 2008. p. 807–816.
[12] T.P. Gabb, J. Gayda, J. Telesman, L.J. Ghosn, A. Garg, Factors influencing dwell fatigue life in notches of a powder metallurgy superalloy, International Journal of Fatigue, 48 (2013) 55-67
[13] R. Jiang, S. Everitt, N. Gao, K. Soady, J.W. Brooks, P.A.S. Reed, Influence of oxidation on fatigue crack initiation and propagation in turbine disc alloy N18, International Journal of Fatigue, 75 (2015) 89-99.
[14] R. Jiang, D.J. Bull, D. Proprentner, B. Shollock, P.A.S. Reed, Effects of oxygen-related damage on dwell-fatigue crack propagation in a P/M Ni-based superalloy: From 2D to 3D assessment, International Journal of Fatigue, 99, Part 1 (2017) 175-186.
[15] H.Y. Li, J.F. Sun, M.C. Hardy, H.E. Evans, S.J. Williams, T.J.A. Doel, P. Bowen, Effects of microstructure on high temperature dwell fatigue crack growth in a coarse grain PM nickel based superalloy, Acta Materialia, 90 (2015) 355-369.
[16] R. Jiang, P.A.S. Reed, Critical Assessment 21: oxygen-assisted fatigue crack propagation in turbine disc superalloys, Materials Science and Technology, 32 (2016) 401-406.
[17] C.F. Miller, G.W. Simmons, R.P. Wei, Mechanism for oxygen enhanced crack growth in inconel 718, Scripta Materialia, 44 (2001) 2405-2410.
[18] J.A. Pfaendtner, C.J. McMahon Jr, Oxygen-induced intergranular cracking of a Ni-base alloy at elevated temperatures—an example of dynamic embrittlement, Acta Materialia, 49 (2001) 3369-3377.
[19] U. Krupp, W.M. Kane, C. Laird, C.J. McMahon, Brittle intergranular fracture of a Ni-base superalloy at high temperatures by dynamic embrittlement, Materials Science and Engineering: A, 387–389 (2004) 409-413.
[20] H.S. Kitaguchi, H.Y. Li, H.E. Evans, R.G. Ding, I.P. Jones, G. Baxter, P. Bowen, Oxidation ahead of a crack tip in an advanced Ni-based superalloy, Acta Materialia, 61 (2013) 1968-1981.
[21] R. Jiang, N. Gao, P.A.S. Reed, Influence of orientation-dependent grain boundary oxidation on fatigue cracking behaviour in an advanced Ni-based superalloy, J Mater Sci, 50 (2015) 4379-4386.
[22] T. P. Gabb, J. Gayda, J. Telesman, Thermal and mechanical property characterization of the advanced disk alloy LSHR. NASA report NASA/TM-2005-213645; 2005.
[23] L. Viskari, M. Hörnqvist, K.L. Moore, Y. Cao, K. Stiller, Intergranular crack tip oxidation in a Ni-base superalloy, Acta Materialia, 61 (2013) 3630-3639.
[24] A. Pineau, S.D. Antolovich, High temperature fatigue of nickel-base superalloys – A review with special emphasis on deformation modes and oxidation, Engineering Failure Analysis, 16 (2009) 2668-2697.
[25] L. Ma, K.-M. Chang, Identification of SAGBO-induced damage zone ahead of crack tip to characterize sustained loading crack growth in alloy 783, Scripta Materialia, 48 (2003) 1271-1276.
[26] H. Ghonem, T. Nicholas, A. Pineau, Elevated temperature fatigue crack growth in alloy 718—part II: effects of environmental and material variables, Fatigue & Fracture of Engineering Materials & Structures, 16 (1993) 577-590.
[27] H. Ghonem, D. Zheng, Depth of intergranular oxygen diffusion during environment-dependent fatigue crack growth in alloy 718, Materials Science and Engineering: A, 150 (1992) 151-160.
[28] A. Karabela, L.G. Zhao, B. Lin, J. Tong, M.C. Hardy, Oxygen diffusion and crack growth for a nickel-based superalloy under fatigue-oxidation conditions, Materials Science and Engineering: A, 567 (2013) 46-57.
[29] L. Viskari, Y. Cao, M. Norell, G. Sjöberg, K. Stiller, Grain boundary microstructure and fatigue crack growth in Allvac 718Plus superalloy, Materials Science and Engineering: A, 528 (2011) 2570-2580.
[30] R. Jiang, N. Karpasitis, N. Gao, P.A.S. Reed, Effects of microstructures on fatigue crack initiation and short crack propagation at room temperature in an advanced disc superalloy, Materials Science and Engineering: A, 641 (2015) 148-159.
[31] T. P. Gabb, J. Telesman, P. T. Kantzos, J. W. Smith, P. F. Browning, Effects of high temperature exposures on fatigue life of disk superalloys. In: K.A. Green, T.M. Pollock, H. Harada, T.E. Howson, R.C. Reed, J.J. Schirra, and S, Walston, editors. Superalloys 2004. Warrendale (PA): The Minerals, Metals & Materials Society; 2004. p. 269–274.

[32] C.K. Sudbrack, S.L. Draper, T.T. Gorman, J. Telesman, T.P. Gabb, D.R. Hull, Oxidation and the Effects of High Temperature Exposures on Notched Fatigue Life of an Advanced Powder Metallurgy Disk Superalloy, in: Superalloys 2012, John Wiley & Sons, Inc., 2012, pp. 863-872.
[33] S. Cruchley, H.Y. Li, H.E. Evans, P. Bowen, D.J. Child, M.C. Hardy, The role of oxidation damage in fatigue crack initiation of an advanced Ni-based superalloy, International Journal of Fatigue, 81 (2015) 265-274.
[34] A.A.N. Németh, D.J. Crudden, D.E.J. Armstrong, D.M. Collins, K. Li, A.J. Wilkinson, C.R.M. Grovenor, R.C. Reed, Environmentally-assisted grain boundary attack as a mechanism of embrittlement in a nickel-based superalloy, Acta Materialia, 126 (2017) 361-371.
[35] H.E. Evans, H.Y. Li, P. Bowen, A mechanism for stress-aided grain boundary oxidation ahead of cracks, Scripta Materialia, 69 (2013) 179-182.
[36] C.F. Miller, G.W. Simmons, R.P. Wei, Evidence for internal oxidation during oxygen enhanced crack growth in P/M Ni-based superalloys, Scripta Materialia, 48 (2003) 103-108.
[37] H.S. Kitaguchi, M.P. Moody, H.Y. Li, H.E. Evans, M.C. Hardy, S. Lozano-Perez, An atom probe tomography study of the oxide–metal interface of an oxide intrusion ahead of a crack in a polycrystalline Ni-based superalloy, Scripta Materialia, 97 (2015) 41-44.
[38] R. Jiang, N. Gao, M. Ward, Z. Aslam, J. C. Walker, P. A. S. Reed. Effects of oxidation on fatigue crack initiation and propagation in an advanced disk alloy. In: M. Hardy, E. Huron, U. Glatzel, B. Griffin, B. Lewis, C. Rae, V. Seetharaman, S. Tin, editors. Superalloys 2016. Seven Springs (PA): The Minerals, Metals & Materials Society; 2016. p. 907–916.
[39] U. Krupp, K. Wackermann, H.-J. Christ, M.H. Colliander, K. Stiller, Intergranular Oxidation Effects During Dwell-Time Fatigue of High-Strength Superalloys, Oxid Met, 88 (2017) 3-14.
[40] D. Bika, C.J. McMahon Jr, A model for dynamic embrittlement, Acta Metallurgica et Materialia, 43 (1995) 1909-1916.
[41] M. Hörnqvist, L. Viskari, K.L. Moore, K. Stiller, High-temperature crack growth in a Ni-base superalloy during sustained load, Materials Science and Engineering: A, 609 (2014) 131-140.
[42] H.V. Atkinson, A review of the role of short-circuit diffusion in the oxidation of nickel, chromium, and nickel-chromium alloys, Oxid Met, 24 (1985) 177-197.
[43] A. Karabela, L.G. Zhao, J. Tong, N.J. Simms, J.R. Nicholls, M.C. Hardy, Effects of cyclic stress and temperature on oxidation damage of a nickel-based superalloy, Materials Science and Engineering: A, 528 (2011) 6194-6202.
[44] L.Y. Xu, Y.F. Cheng, Corrosion of X100 pipeline steel under plastic strain in a neutral pH bicarbonate solution, Corrosion Science, 64 (2012) 145-152.
[45] H.J. Christ, K. Wackermann, U. Krupp, Effect of dynamic embrittlement on high temperature fatigue crack propagation in IN718 – experimental characterisation and mechanism-based modelling, Materials at High Temperatures, 33(2016) 528-535.
[46] D. Hu, J. Mao, J. Song, F. Meng, X. Shan, R. Wang, Experimental investigation of grain size effect on fatigue crack growth rate in turbine disc superalloy GH4169 under different temperatures, Materials Science and Engineering: A, 669 (2016) 318-331.
[47] S. Suresh, Fatigue of Materials, 2nd edition, Cambridge University Press, Cambridge, 1998.
[48] S.L. Semiatin, K.E. McClary, A.D. Rollett, C.G. Roberts, E.J. Payton, F. Zhang, T.P. Gabb, Microstructure Evolution during Supersolvus Heat Treatment of a Powder Metallurgy Nickel-Base Superalloy, Metall and Mat Trans A, 43 (2012) 1649-1661.
[49] T. P. Gabb, J. Gayda, J. Telesman, A. Garg, The effects of heat treatment and microstructure variations on disk superalloy properties at high temperature. In: R.C. Reed, K. A. Green, P. Caron, T. P. Gabb, M. G. Fahrmann, E. S. Huron, S. A. Woodard, editors. Superalloys 2008. Warrendale (PA): The Minerals, Metals & Materials Society; 2008. p. 121-130.
[50] R. Jiang, Study of Fatigue Crack Initiation and Propagation Mechanisms in an Advanced Ni-based Superalloy: Effects of Microstructures and Oxidation, PhD theses, (2015).
[51] W.C. Oliver, G.M. Pharr, Nanoindentation in materials research: Past, present, and future, Mrs Bulletin, 35 (2010) 897-907.
[52] R. Jiang, F. Pierron, S. Octaviani, P.A.S. Reed, Characterisation of strain localisation processes during fatigue crack initiation and early crack propagation by SEM-DIC in an advanced disc alloy, Materials Science and Engineering: A, 699 (2017) 128-144.

[53] P.M. Scott, T.W. Thorpe, A critical review of crack tip stress intensity factors for semi-elliptic cracks, Fatigue & Fracture of Engineering Materials & Structures, 4 (1981) 291-309.
[54] N. Birks, G. H. Meier, F. S. Pettit, Introduction to the High Temperature Oxidation of Metals, Cambridge University Press, 2nd edition, 2009.
[55] X. Fang, X. Dong, D. Jiang, X. Feng, Modification of the mechanism for stress-aided grain boundary oxidation ahead of cracks, Oxid Met, 89 (2018) 1-8.